The Microstructure and Environmental Resistance of Low-Cr ODS FeCrAl

K. A. Unocic*, D. T. Hoelzer and B. A. Pint
Materials Science and Technology Division
Oak Ridge National Laboratory
*e-mail: unocicka@ornl.gov

Three oxide dispersions strengthened (ODS) Fe-12at.%Cr-9at.% (5wt.%)Al alloys were mechanically alloyed with different oxide additions: (1) Y_2O_3, (2) Y_2O_3 + HfO_2, and (3) Y_2O_3 + ZrO_2. The as-extruded microstructure was characterized including the oxide particle composition and size distribution. The 700°C Pb-Li compatibility was evaluated for a fusion energy application and the steam oxidation resistance at 1200°C and higher temperatures was evaluated for a nuclear accident tolerant fuel cladding application. The alloy containing only Y_2O_3 contained some low-Al regions and did not perform well but provides a baseline. The other alloys contain sufficient Cr and Al to form a protective $LiAlO_2$ surface oxide, which inhibits dissolution in Pb-Li. Also, a protective α-Al_2O_3 scale formed in steam oxidation at 1200°C, similar to the scale formed in dry air at 1200°C. For the alloy with HfO_2, the scale remained protective to 1475°C in steam..

Key words: ODS, FeCrAl, Al_2O_3, liquid metal compatibility, steam oxidation, oxide grain boundary segregation

INTRODUCTION

In recent years, ferritic oxide dispersions strengthened (ODS) alloys have become attractive for both nuclear fusion and fission applications because it was discovered that a microstructure with a fine stable oxide dispersion was very resistant to radiation damage mechanisms, especially the severe environment needed to commercialize fusion energy [1-4]. While the initial focus has been mainly on ODS FeCrW compositions, the addition of Al has been found to have an extreme benefit on corrosion environments ranging from liquid metals to supercritical water [5-8]. The additional interest in accident tolerant fuel concepts to increase the safety margin in conventional nuclear reactors has increased the range of environments to >1200°C steam during a beyond design basis accident scenario

[9]. In this case, ODS Fe-15Cr alloys do not provide sufficient protection above 1000°C in steam and Al-containing ODS alloys offer low reaction rates to over 1400°C [10]. Research on FeCrAl alloys for cladding is ~50 years old and ODS FeCrAl was first commercialized more than 30 years ago [11,12].

Prior work on model FeCrAlY alloys identified Fe-12wt%Cr-5wt.%Al (12at.%Cr-9.5%Al) as being compatible with both Pb-Li [13] and 1200°C steam [14]. The Cr content was kept lower than normal in FeCrAl alloys to reduce the possibility of embrittlement from irradiation induced α′ formation (reviewed previously [9]). Typically, Cr levels are near 20% for the most oxidation resistant FeCrAl alloys in order to assist the formation of alumina [15]. Three different versions were prepared with different oxide dispersions in order to investigate the stability of multi-cation oxide precipitates [16]. The current study examined the steam oxidation resistance and Pb-Li compatibility of these initial alloys with nominally 12%Cr-5wt.%(9.5at.%)Al. The results are promising with good performance observed in both environments even with this low level of Cr in the alloy. However, more work is needed to understand and optimize the processing of these alloys and to identify how changes in the oxide additions may be affecting performance.

EXPERIMENTAL PROCEDURE

Three ODS FeCrAl alloys were ball milled in a Zoz model CM08 1kg powder batches using the same pre-alloyed powder with the following oxide additions: (1) Y_2O_3 (125Y) (2) Y_2O_3 + ZrO_2 (125YZ) and (3) Y_2O_3 + HfO_2 (125YH). Milled powders were extruded in mild steel cans after soaking for 1h at 950°C. All specimens were cut from the as-extruded material and the compositions are shown in Table 1. The compositions are listed in at.% to compared the cation additions. The highest C and N impurities and lowest Cr and Al contents were in the 125Y, which was milled first and was slightly contaminated from prior powder that could not be completely removed from the mill. This alloy also had the lowest oxide addition and therefore had the lowest O content. For comparison, the compositions of several other ODS alloys are included in Table 1 as well as wrought FeCrAl alloys used for comparison.

Two different types of environmental testing were conducted: (1) 1000h isothermal exposures in Pb-Li at 700°C in a welded Mo capsule and (2) high temperature oxidation exposures in air and steam at 1200°C and higher temperatures. The capsule tests used 125 g of eutectic Pb~15-17at.%Li and the procedure has been described elsewhere [6,13]. Each ODS FeCrAl specimen is held in a separate Mo capsule, which is used as it is inert to dissolution in Pb-Li. The capsules were loaded in a glove box and welded shut to minimize impurity ingress during the 1000 h experiment. The Mo capsule was welded inside a larger type 304 stainless steel capsule to protect the Mo from oxidizing. After exposure, residual Pb-Li on the specimen surface was removed by soaking in a 1:1:1 mixture of acetic acid, hydrogen peroxide and ethanol for up to 72h. The high temperature oxidation testing was all conducted in a magnetic suspension Rubotherm model DynTHERM LP-HT-II thermal gravimetric analysis (TGA) instrument where the alumina test chamber was fully isolated from the balance and isothermal experiments were conducted at 1200°C with dry air or 100% steam. In order to explore higher temperature behavior in steam and simulate an accident environment, specimens were "ramp" tested with steam introduced at 600°C and the specimen heated at 5°C/min until the mass gain indicated breakaway oxidation. At that point, the ramp was immediately stopped (manually) and the specimen cooled to room temperature. In both experiments, the alloy coupons were ~1.5x10x19 mm and were polished to a 600 grit SiC finish and cleaned ultrasonically in acetone and methanol. Mass changes were recorded before and after exposures in a Mettler-Toledo model XP205 balance with an accuracy of 0.01mg/cm^2.

After exposure, the specimens were characterized using x-ray diffraction (XRD) and secondary electron microscopy (SEM) (Hitachi models S3400 and S4800) equipped with energy dispersive x-ray (EDX) analysis. Prior to metallographic sectioning, specimens were Cu-plated to protect the surface oxide. Polished cross-sections were examined by light microscopy, SEM and electron probe microanalysis (EPMA) using wavelength dispersive x-ray analysis. Transmission electron microscope (TEM) specimens were prepared via the focus ion beam (FIB) in-situ lift-out technique using a Hitachi NB5000 FIB-SEM. Thinned specimens were examined by (1) scanning-transmission electron microscopy (STEM) (Philips model CM200) with a Schottky field

emission gun (FEG) operated at 200kV and EDX, (2) JEOL 2200FS-AC STEM also with a FEG 200kV corrected probe (using CEOS C_s-Corrector) with 0.7Å resolution and a Bruker XFlash® 6|30 SDD.

RESULTS

Alloy Microstructure

Examples of the as-extruded microstructures are shown with SEM backscattered electron (BSE) and STEM high angle annular dark field (HAADF) images in Figure 1. A summary of grain size and hardness is provided in Table 2. The largest grain size (0.83 μm) was found in the base 125Y alloy and the smallest in the 125YZ alloy. Bi-modal particle size distributions were observed in 125Y(Fig. 1b) and 125YZ (Fig. 1f), while a trimodal particle size distribution was found in 125YH (Fig. 1d) [16]. The STEM analysis showed that all of the heats contained a high concentration of nano-size (<5 nm diameter) oxide particles in the grain interiors (Figures 1b, 1d and 1f) and confirmed by the Fe jump ratio (representative example in Figure 1h for 125YH). The EDS maps in Figure 1g show that some precipitates contain both Y and Hf suggesting the existence of cubic $Y_2Hf_2O_7$. Table 2 also shows the average particle sizes measured in each alloy with 125Y having the smallest (2.43 nm) and 125YH the largest (3.18 nm). In addition to the fine precipitates, the lower magnification images show the presence of defects and larger oxide particles, Figures 1a, 1c and 1e.. Alloy 125Y had the lowest room temperature hardness, Table 2, possibly because of the lower oxide volume, which also resulted in the lowest tensile properties among the three as-extruded materials [16].

Pb-Li Compatibility

The mass change data for the new ODS alloys after 1000 h at 700°C in static Pb-Li is summarized in Figure 2. For reference, the mass change for several cast FeCrAl alloys [13] is shown as well as other ODS alloys with and without Al, Table 1. When Al is present in the alloy, a $LiAlO_2$ layer is formed on the specimen [6] from O impurities in the Pb-Li (200-400ppmw as cast) and this layer inhibits dissolution into the liquid metal. The high mass loss for the 125Y specimen was linked to spalled $LiAlO_2$ surface oxide and (~300μm) pits in the surface (Figure 3), which suggest that powder with littler or no Al was incorporated in this first batch of material and was selectively dissolved from the

specimen. Similar extreme behavior was observed when an aluminized 9Cr steel specimen was exposed with one cut (uncoated) face [17]. Both Fe and Cr have a high solubility in Pb-Li and without the Al to form a stable oxide, dissolution occurs rapidly without the liquid reaching saturation thereby slowing the dissolution rate. Surprisingly, the 125YH specimen also showed similar mass loss as the 125Y specimen but without any indication of significant dissolution or spallation. The 125YZ specimen showed the lowest mass change, which was consistent with the cast FeCrAl alloys of similar composition, Figure 2. The higher mass loss for the cast alloy with only 4wt.%Al indicated that the Al content could not be reduced below ~5wt.%Al for this application. Similar to several previous results [6,13,17,18], XRD identified the surface reaction product for each specimen as $LiAlO_2$.

Isothermal High-Temperature Oxidation

Figure 4 summarizes the 1200°C isothermal results in air and steam. Again, 125Y showed the worst behavior with a very high mass gain observed in steam with the formation of Fe-rich oxide nodules. Even in dry air, the mass gain was nearly linear and higher than the other alloys. The other alloys, 125YH and 125YZ, both showed low mass gains in both air and steam, similar to the behavior of commercial alloy APMT, Table 1. The mass change data was more erratic in steam, likely due to the low mass changes being measured and perhaps some minor water condensation occurring at the top of the reaction chamber where the temperature was lower. The minor differences observed between air and steam is consistent with previous observations of alumina-forming alloys and coatings in air with and without 10-90%H_2O [19-23].

The scale surfaces after steam and air exposures at 1200°C were examined. Little difference was noted between the two environments and Figure 5 shows examples from the exposures in steam. Figure 5a shows large spalled areas on the surface of the 125Y specimen. At the gas interface of the scale formed on this alloy, Y-rich oxide particles were observed but they were not uniformly distributed, Figure 5b. The formation of these Y-rich precipitates is consistent with the outward diffusion of Y from the substrate [24,25]. For the co-doped alloys, both Y and Hf or Zr oxides were observed more uniformly distributed at the gas interface, Figures 5c and 5d.

Figure 6 shows cross-sections of the alumina scales formed in air and steam at 1200°C and measurements of the oxide thicknesses are provided in Table 3. The oxide thicknesses in steam were very similar for the three new ODS alloys. Consistent with the high mass gain shown in Figure 4, 125Y also formed Fe-rich oxide nodules in some areas. These measurements focused on the regions that formed adherent alumina. The scales on the new alloys were all thicker than the scales formed on APMT and cast and rolled FeCrAlY in steam, Figures 6g and 6h. The scales formed in air on 125YH and 125YZ were similar in thickness and appearance to those formed in steam, Figures 6c-6f. However, the scale formed in air on 125Y was thinner, Figures 6a and 6b. The thicker scale formed on the co-doped ODS alloys may be due to "over-doping" of the alloy with much higher levels of dopant additions in 125YH and 125YZ compared to APMT or PM2000, Table 1. High levels of dopants have been found to accelerate the oxide scale formation rate in both wrought and ODS alumina-forming alloys [26-29]. The Hf- and Zr- rich oxide precipitates can be clearly seen in the scales formed on 125YH and 125YZ and these are fast oxygen conductors, allowing rapid transport through the scale compared to the slow diffusion expected in α-Al_2O_3 [30]. Interestingly, large interfacial voids were observed on all of the new ODS alloys (arrows in Figure 6) with the highest volume observed for 125YH. No similar voids were observed on APMT or wrought FeCrAlY. Small interfacial voids are common in ODS alloys [25,31], but these are somewhat larger than prior observations.

In order to study the alumina scale grain structure and interfacial voids, TEM cross-sections were made of the same specimens. Figure 7 compares the microstructures of the three new ODS alloys after oxidation in steam. The typical two-layer alumina structure was observed with equiaxed grains in the outer layer and more columnar grains in the inner layer, reflecting the inward growth of the doped alumina scales [18,22-29,31-33]. Using various identification techniques (XRD, EBSD, and electron diffraction analysis) it was confirmed that both layers were α-Al_2O_3. The most unusual structure was observed for the 125YH specimen, Figure 7b. The interfacial voids, consistent with the polished cross-sections, were much larger for this specimen and the inner grain structure was disrupted. No Y-rich precipitates were observed in the 125Y cross-section. However, HfO_2 and $Y_2Hf_2O_7$ were observed in the oxide scale formed on 125YH, while

$YZrO_3$ and ZrO_2 were present in the scale formed on 125YZ. For comparison, the scale formed in air on 125YH is shown in Figure 8. A similar grain structure was observed, however, a much larger volume fraction of Y- and Hf-rich oxide particles was present in the section. These phases are seen clearly with the Z-contrast in the high angle annular dark field image in Figure 8b. The polished cross-sections in air and steam both show dopant-rich oxide phases, Figures 6c and 6d, so it is difficult to determine if there is any effect of environment on their formation. Likewise, the interfacial voids were not as large and numerous in this cross-section but this may only reflect local variations in the void population. The inset in Figure 8 shows an example electron diffraction pattern generated from the inner scale and oriented along the $[\bar{2}02\bar{1}]_{\alpha\text{-}Al_2O_3}$ zone axis. A HfO_2 precipitate (marked in Fig. 8b with arrow) was also identified by electron diffraction analysis.

Figure 9 shows images of the 125YH substrate near the air-formed scale interface. Both types of nano-size precipitates were observed. Figure 10 shows a similar observation for the 125Y substrate beneath the scale formed in steam. The EDS maps clearly show the small Y_2O_3 precipitates (and not a Y-Al-O phase) in the substrate matrix close to the metal-oxide interface. The maps also show Y interfacial segregation at an alumina grain boundary and the metal-scale interface, Figure 10. Finally, Figure 11 shows the co-segregation of Y and Zr to the alumina grain boundaries in 125YZ. Co-segregation of Y and Hf also was observed in 125YH, but examples of Y and Hf co-segregation have been reported previously for NiCoCrAlYHfSi bond coatings and model alloys [34-36].

While the 1200°C steam oxidation resistance is an important demonstration for these new alloys, one of the key parameters for an accident tolerant fuel cladding is the maximum temperature where the material can form a protective alumina scale in steam. Thus, a "ramp" test was used to determine this maximum temperature. Figure 12a shows the specimen mass gain as a function of temperature during the 5°C/min heating. Consistent with the high isothermal mass gain for 125Y in steam, the alloy began to show an increased mass gain at relatively low temperatures and the temperature where the specimen had gained 3 mg/cm^2 was 819°C. For the other two ODS alloys, low mass gains were recorded until much higher temperatures. The 125YZ specimen experienced

breakaway oxidation at ~1325°C and the 125YH specimen at ~1475°C, which was better than commercial ODS alloy MA956 and only slightly less than APMT with 22%Cr, Figure 12b. More testing is needed to verify these results and determine why the 125YH specimen showed better performance than the 125YZ specimen. Compared to the wrought FeCrAl [37] and FeCrAlY specimens tested previously, lowering the alloy Cr content appeared to decrease the maximum temperature, consistent with a third element effect [15]. The 125YZ specimen appeared consistent with those results, while the 125YH appeared to outperform that trend. The high mass gain at the end of the ramp reflects the formation of Fe-rich oxide nodules on these specimens and characterization was not performed.

CONCLUSIONS

Three ODS alloys with lower Cr content (~12%) than conventional ODS FeCrAl alloys were ball milled with combinations of Y_2O_3, HfO_2 and ZrO_2. Microstructural differences after processing were observed in grain size and precipitation type, size and distribution. One application for these alloys in a fusion energy blanket requires Pb-Li compatibility. Initial screening at 700°C showed a low mass gain for the 125YZ alloy specimen with Y_2O_3+ ZrO_2, which formed a surface $LiAlO_2$ layer that inhibited dissolution. However, the other two alloys showed mass losses. The 125Y alloy with only Y_2O_3 showed the worst performance, suggesting contamination during the milling process. A second application as accident tolerant fuel cladding requires high temperature steam oxidation resistance. Again the 125Y alloy specimens showed poor performance at 1200°C. The co-doped alloys with ZrO_2 and HfO_2 formed protective α-Al_2O_3 scales at 1200°C in steam. The mass gain and microstructures were remarkably similar in dry air and steam at 1200°C, showing similar grain structures, dopant-rich oxide phases and grain boundary and interfacial segregation consistent with prior observations. At higher temperature steam oxidation testing the 125YH alloy was protective to ~1475°C, a very promising result for these low Cr alloys.

ACKNOWLEDGMENTS

The authors would like to thank D.W. Coffey, M.S. Stephens, M. Howell, T.M. Lowe, and T. Geer for assistance with the experimental work. J.R. Keiser, R.R. Unocic, C. Parrish and S. Pawel provided comments and suggestions on the results and manuscript. This research was funded by U.S. Department of Energy (DOE), Office of Fusion Energy Sciences, Fusion Energy Materials Program and the U.S. Department of Energy's Office of Nuclear Energy, Advanced Fuel Campaign of the Fuel Cycle R&D program and by the Center for Nanophase Materials Sciences (CNMS), which is sponsored by the Scientific User Facilities Division, Office of Basic Energy Sciences, U.S. Department of Energy.

REFERENCES

[1] S. Ukai, T. Nishida, T. Okuda and T. Yoshitake, "R&D of Oxide Dispersion Strengthened Ferritic Martensitic Steels for FBR," *J. Nucl. Mater*. **263**, 1745-1749 (1998).

[2] S. Ukai and M. Fujiwara, "Perspective of ODS Alloys Application in Nuclear Environments," *J. Nucl. Mater*. **307**, 749-757 (2002).

[3] T. Yamamoto, G. R. Odette, P. Miao, D. T. Hoelzer, J. Bentley, N. Hashimoto, H. Tanigawa, and R. J. Kurtz, "The transport and fate of helium in nanostructured ferritic alloys at fusion relevant He/dpa ratios and dpa rates," *J. Nucl. Mater*. **367**, 399-410 (2007).

[4] D. A. McClintock, M. A. Sokolov, D. T. Hoelzer and R. K. Nanstad, "Mechanical properties of irradiated ODS-EUROFER and nanocluster strengthened 14YWT," *J. Nucl. Mater*. **392**, 353-359 (2009).

[5] A. Kimura, R. Kasada, N. Iwata, H. Kishimoto, C.H. Zhang, J. Isselin, P. Dou, J.H. Lee, N. Muthukumar, T. Okuda, M. Inoue, S. Ukai, S. Ohnuki, T. Fujisawa and T. F. Abe, "Development of Al added high-Cr ODS steels for fuel cladding of next generation nuclear systems," *J. Nucl. Mater*. **417**, 176-179 (2011).

[6] B. A. Pint, L. R. Walker and K. A. Unocic, "Material Compatibility with Isothermal Pb-Li," *Mater. High Temp.* **29**, 129-135 (2012).

[7] S. Takaya, T. Furukawa, G. Müller, A. Heinzel, A. Jianu, A. Weisenburger, K. Aoto, M. Inoue, T. Okuda, F. Abe, S. Ohnuki, T. Fujisawa and A. Kimura, "Al-containing ODS steels with improved corrosion resistance to liquid lead–bismuth," *J. Nucl. Mater*. **428**, 125-130 (2012).

[8] J. Lim, I. S. Hwang and J. H. Kim, "Design of alumina forming FeCrAl steels for lead or lead–bismuth cooled fast reactors," *J. Nucl. Mater*. **441**, 650-660 (2013).

[9] K.A. Terrani, S.J. Zinkle, L.L. Snead, "Advanced oxidation-resistant iron-based alloys for LWR fuel cladding ," *J. Nucl. Mater*. **448**, 420-435 (2014).

[10] B. A. Pint, K. A. Terrani M. P. Brady, T. Cheng and J. R. Keiser, "High Temperature Oxidation of Fuel Cladding Candidate Materials in Steam-Hydrogen Environments," *J. Nucl. Mater*. **440**, 420-427 (2013).
[11] C. S. Wukusick and J. F. Collins, "An Iron-Chromium-Aluminum Alloy Containing Yttrium," *Materials Research Standard* **4**, 637-46 (1964).
[12] J. D. Whittenberger, "Tensile and Creep Properties of the Experimental Oxide Dispersion Strengthened Iron-Base Sheet Alloy MA-956E at 1365K," *Met. Trans. A* **9**, 101-110 (1978).
[13] K. A. Unocic and B. A. Pint, ""Alloying and Coating Strategies for Improved Pb-Li Compatibility," *J. Nucl. Mater*. accepted for publication (2014).
[14] B. A. Pint, K. A. Terrani, J. R. Keiser, M. P. Brady, Y. Yamamoto and L. L. Snead, "Material Selection for Fuel Cladding Resistant to Severe Accident Scenarios," NACE Paper ED2013-3083, Houston, TX, presented at the 16th Environmental Degradation conference, Asheville, NC, August 2013.
[15] F. H. Stott, G. C. Wood and J. Stringer, "The Influence of Alloying Elements on the Development and Maintenance of Protective Scales," *Oxid. Met.* **44**, 113-145 (1995).
[16] D. T. Hoelzer, K. A. Unocic and D. Shin, "Development of ODS FeCrAl Ferritic Alloys for Fusion Reactor Applications: Comparison of Computational and Experimental Studies," submitted to *J. Nucl. Mater*. (2014).
[17] B. A. Pint and K. A. Unocic, "Pb-Li Compatibility Issues for DEMO," *J. Nucl. Mater*. **442**, 572-575 (2013).
[18] B. A. Pint and K. L. More, "Transformation of Al_2O_3 to $LiAlO_2$ in Pb-17Li at 800°C," *J. Nucl. Mater*. **376**, 108-113 (2008).
[19] H. Al-Badairy and G J Tatlock, "The Influence of the Moisture Content of the Atmosphere on Alumina Scale Formation and Growth During High Temperature Oxidation of PM2000," *Mater. High Temp*. **17**, 133-137 (2000).
[20] J. Engkvist, S. Canovic, K. Hellström, A. Järdnäs, J.-E. Svensson, L.-G. Johansson, M. Olsson and M. Halvarsson, "Alumina Scale Formation on a Powder Metallurgical FeCrAl Alloy (Kanthal APMT) at 900–1,100°C in Dry O_2 and in O_2 + H_2O," *Oxid. Met.* **73** (2010) 233-253.
[21] D. J. Young, D. Naumenko, L. Niewolak, E. Wessel, L. Singheiser and W. J. Quadakkers, "Oxidation kinetics of Y-doped FeCrAl-alloys in low and high pO_2 gases," *Mater. Corr*. **61** (2010) 838-844.
[22] K. A. Unocic, E. K. Essuman, S. Dryepondt, and B. A. Pint, "Effect of Environment on the Scale Formed on ODS FeCrAl at 1100°C," *Mater. High Temp*. **29**, 171-180 (2012).
[23] K. A. Unocic and B. A. Pint, "Effect of Water Vapor on Thermally Grown Alumina Scales on Bond Coatings," *Surf. Coat. Technol.* **215**, 30-38 (2013).
[24] B. A. Pint, A. J. Garratt-Reed and L. W. Hobbs, "The Reactive Element Effect in Commercial ODS FeCrAl Alloys," *Mater. High Temp.* **13**, 3-16 (1995).
[25] B. A. Pint, "Experimental Observations in Support of the Dynamic Segregation Theory to Explain the Reactive Element Effect," *Oxid. Met.* **45**, 1-37 (1996).
[26] B. A. Pint and K. B. Alexander, "Grain Boundary Segregation of Cation Dopants in α-Al_2O_3 Scales," *J. Electrochem. Soc.* **145** , 1819-1829(1998).

[27] B. A. Pint, "The Oxidation Behavior of Oxide-Dispersed β-NiAl: I. Short-Term Cyclic Data and Scale Morphology," *Oxid. Met.* **49**, 531-560 (1998).
[28] B. A. Pint, "Optimization of Reactive Element Additions to Improve Oxidation Performance of Alumina-Forming Alloys," *J. Am. Ceram. Soc.* **86** , 686-695 (2003).
[29] D. Naumenko, V. Kochubey, L. Niewolak, A. Dymiati, J. Mayer, L. Singheiser and W. J. Quadakkers, "Modification of alumina scale formation on FeCrAlY alloys by minor additions of group IVa elements," J. Mater. Sci. **43**, 4550-4560 (2008).
[30] H. Hindam and D. P. Whittle, "Peg Formation by Short-Circuit Diffusion in Al_2O_3 Scales Containing Oxide Dispersions," *J. Electrochem. Soc*. **129**, 1147-1149 (1982).
[31] B. A. Pint, "On the Formation of Interfacial and Internal Voids in α-Al_2O_3 Scales," *Oxid. Met.* **48**, 303-328 (1997).
[32] F. A. Golightly, F. H. Stott and G. C. Wood, "The Relationship Between Oxide Grain Morphology and Growth Mechanisms for Fe-Cr-Al and Fe-Cr-Al-Y Alloys," *J. Electrochem. Soc.* **126**, 1035-1042 (1979).
[33] W. J. Quadakkers, H. Holzbrecher, K. G. Briefs and H. Beske, "Differences in Growth Mechanisms of Oxide Scales Formed on ODS and Conventional Wrought Alloys," *Oxid. Met.* **32**, 67-88 (1989).
[34] K. A. Unocic and B. A. Pint, "Characterization of the Alumina Scale Formed on a Commercial MCrAlYHfSi Coating," *Surf. Coat. Technol.* **205**, 1178-1182 (2010).
[35] K. A. Unocic, C. M. Parish and B. A. Pint, "Characterization of the Alumina Scale formed on Coated and Uncoated Doped Superalloys," *Surf. Coat. Technol.* **206**, 1522-1528 (2011).
[36] K. A. Unocic and B. A. Pint, (2013) "Oxidation Behavior of Co-Doped NiCrAl Alloys in Dry and Wet Air," *Surf. Coat. Technol.* **237**, 8-15 (2013).
[37] B. A. Pint and R. B. Rebak, unpublished research (2014).

Figure Captions

Figure 1. BSE SEM (a,c,e) and HAADF STEM (b,d,f) images of the as-extruded microstructures of 125Y (a,b), 125YH (c,d), 125YZ (e,f). (g) shows EDS maps from 125YH and (h) shows an Fe jump ratio image from 125YH.

Figure 2. Specimen mass change for alloy specimens exposed for 1000h at 700°C in static Pb-Li.

Figure 3. Light microscopy of the 125Y specimen after 1000 h in Pb-Li at 700°C.

Figure 4. Specimen mass gain as a function of exposure time for the three ODS FeCrAl alloys exposed at 1200°C in air and steam (closed symbols). The mass gain in steam was very similar to that observed for commercial alloy APMT.

Figure 5. Plan view BSE SEM images of the scale formed after 4h at 1200°C in steam on specimens of (a,b) 125Y, (c) 125YH and (d) 125YZ.

Figure 6. SEM BSE images of polished cross-sections after 4h exposures: a) 125Y in steam, b) 125Y in air, c) 125YH in steam, d) 125YH in air, e) 125YZ in steam, f) 125YZ in air, g) cast and rolled 125Y in steam, h) APMT in steam.

Figure 7. STEM bright field images of oxide cross-sections formed in steam after 4h at 1200°C on specimens of a) 125Y, b) 125YH, and c) 125YZ.

Figure 8. STEM (a) bright field and (b) annular dark field images of the scale cross-section formed on 125YH after 4h in air at 1200°C. Inset shows an indexed electron diffraction pattern from the inner oxide layer.

Figure 9. STEM (a) bright field and (b) annular dark field images of the 125YH substrate adjacent to the scale formed after 4h in air at 1200°C.

Figure 10. STEM (a) bright field image of the metal-oxide interface of 125Y after 4h at 1200°C in steam with EDS maps for Al, O, Y, Fe and Y+O map confirming presence of Y_2O_3 precipitates in the substrate near the thermally grown alumina scale.

Figure 11. STEM (a) HAADF image of the oxide scale formed on the 125YZ specimen exposed for 4h at 1200°C in steam with the marked area used for EDS maps of Zr and Y.

Figure 12. a) Specimen mass gain as a function of temperature during the TGA ramp test in steam and (b) the maximum temperature capability as a function of alloy Cr content for the ODS alloys and other commercial and model alloys.

Table 1. Chemical composition (at.%) determined by Inductively Coupled Plasma Atomic Emission Spectroscopy (ICP-AES). Values for Y, O, N, C, S in ppma.

Material	Fe	Cr	Al	Y	N	C	S	O	Others
Powder									
125Y	78.3	11.5	9.3	1120	1710	1660	33	2760	
125YHf	77.5	11.8	9.4	1010	410	960	16	7500	2000Hf-60Zr
125YZr	77.8	11.6	9.5	1060	600	1090	16	6290	30Hf-1730Zr
125cast	79.1	12.2	8.7	160	30	220	21	60	0.02Si
APMT	65.2	21.3	9.7	1481	1512	1315	<16	1731	1.6Mo-0.1Ni-1.1Si-0.068Hf-0.058Zr
14YWT	83.3	14.1	0.04	1240	5166	3001	69	5997	0.59W
PM2000	69.0	19.1	10.5	2280	319	61	13	8056	0.02Ni-0.04Si-0.52Ti

Table 2. Measurements of the grain size and hardness for the as-extruded ODS FeCrAl alloys with commercial PM2000 included for comparison.

Material	**Grain size** [μm]	**Hardness** [HV]	**Particle size** [nm]
125Y	0.83±0.17	365.1	2.43±0.36
125YH	0.70±0.16	419.8	3.18±0.51
125YZ	0.27±0.06	470.0	2.91±0.32
PM2000		356.4	

Table 3. Measured scale thickness

Condition	**125Y** [μm]	**125YH** [μm]	**125YZ** [μm]	**APMT** [μm]	**Cast 125Y** [μm]
1200°C/Air	1.53±0.5	2.23±0.2	2.41±0.2	-	-
1200°C/Steam	2.26±0.3	2.18±0.3	2.34±0.1	1.3±0.2	1.82±0.2

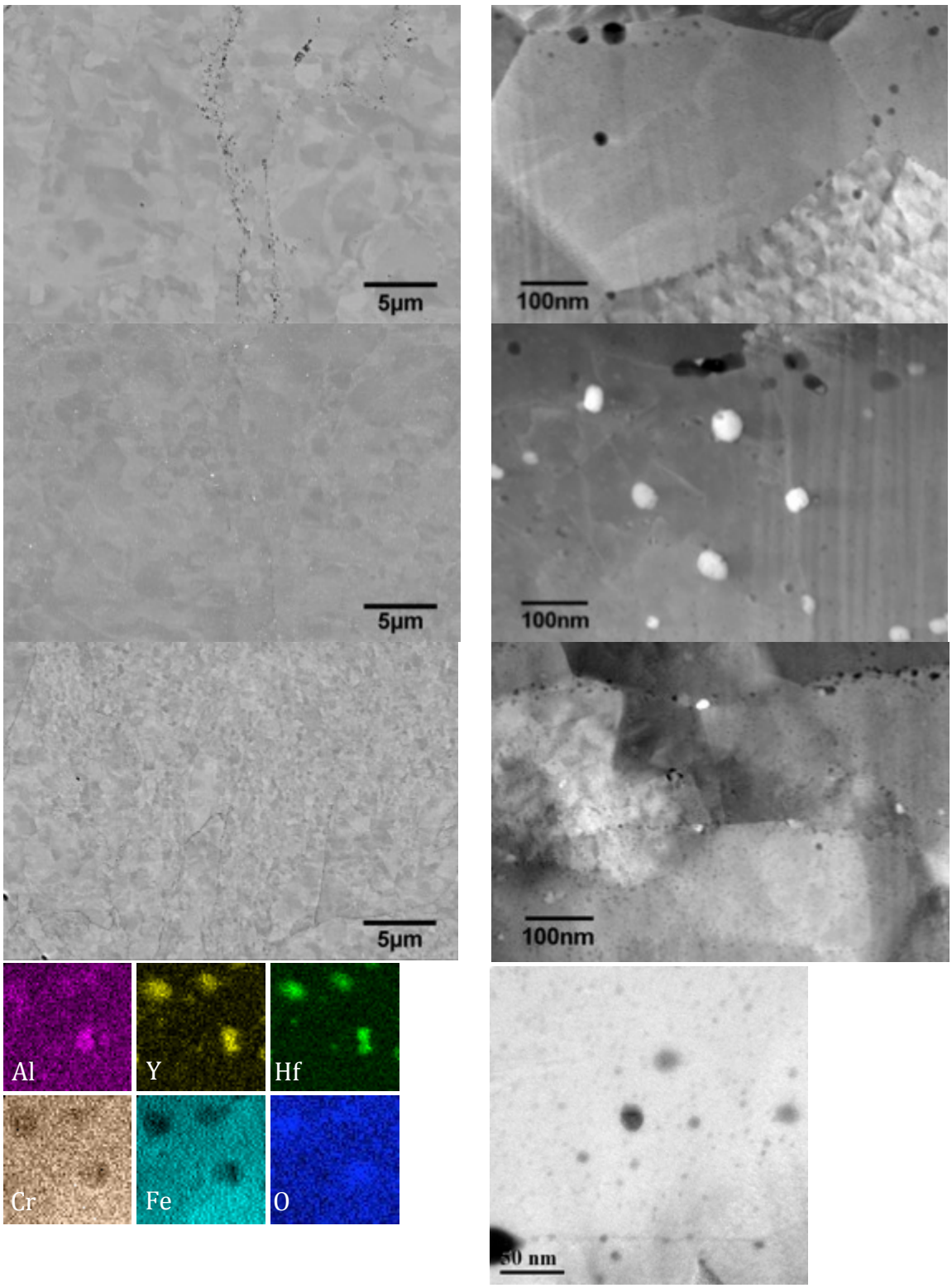

Figure 1. BSE SEM (a,c,e) and HAADF STEM (b,d,f) images of the as-extruded microstructures of 125Y (a,b), 125YH (c,d), 125YZ (e,f). (g) shows EDS maps from 125YH and (h) shows an Fe jump ratio image from 125YH.

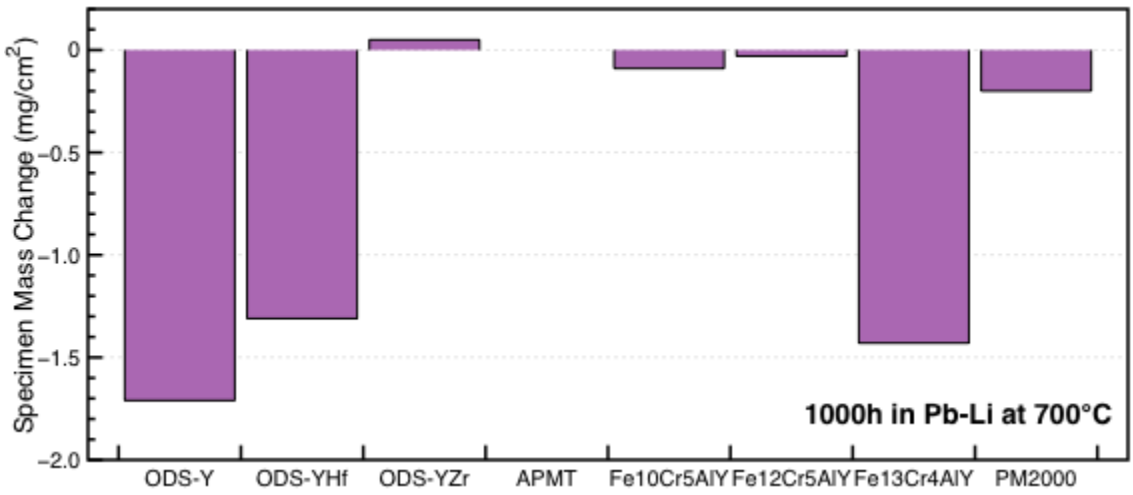

Figure 2. Specimen mass change for alloy specimens exposed for 1000h at 700°C in static Pb-Li.

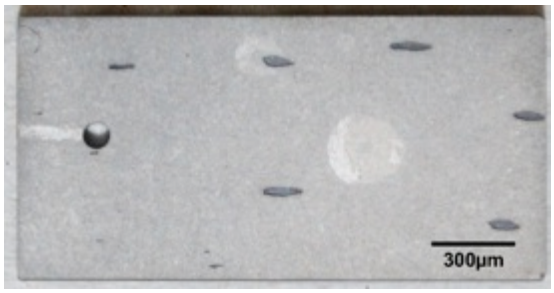

Figure 3. Light microscopy of the 125Y specimen after 1000 h in Pb-Li at 700°C.

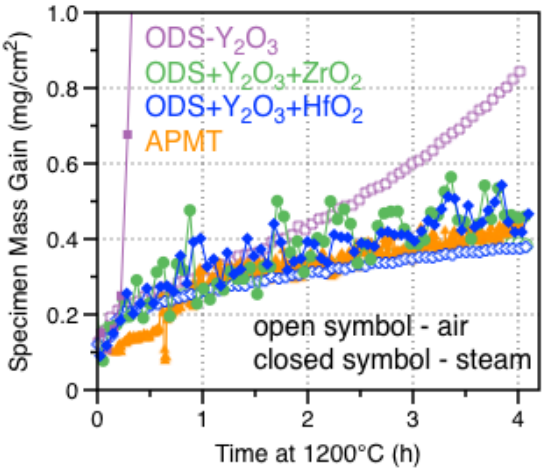

Figure 4. Specimen mass gain as a function of exposure time for the three ODS FeCrAl alloys exposed at 1200°C in air and steam (closed symbols). The mass gain in steam was very similar to that observed for commercial alloy APMT.

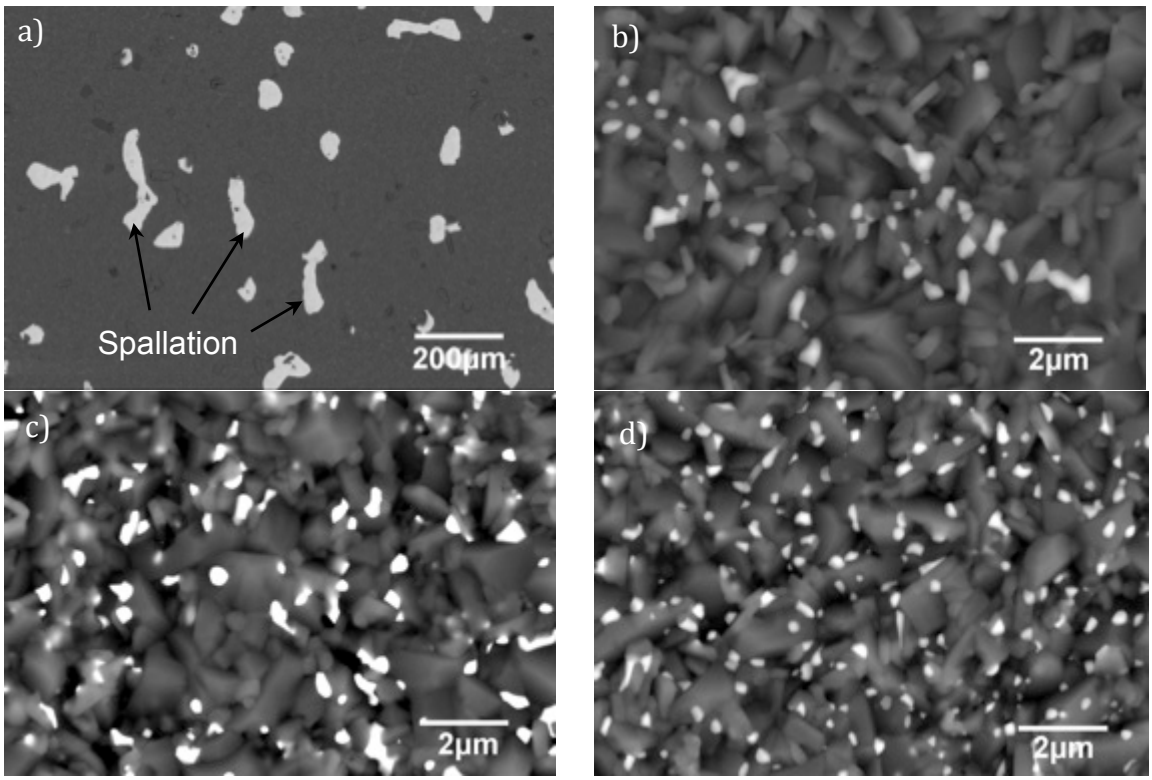

Figure 5. Plan view BSE SEM images of the scale formed after 4h at 1200°C in steam on specimens of (a,b) 125Y, (c) 125YH and (d) 125YZ.

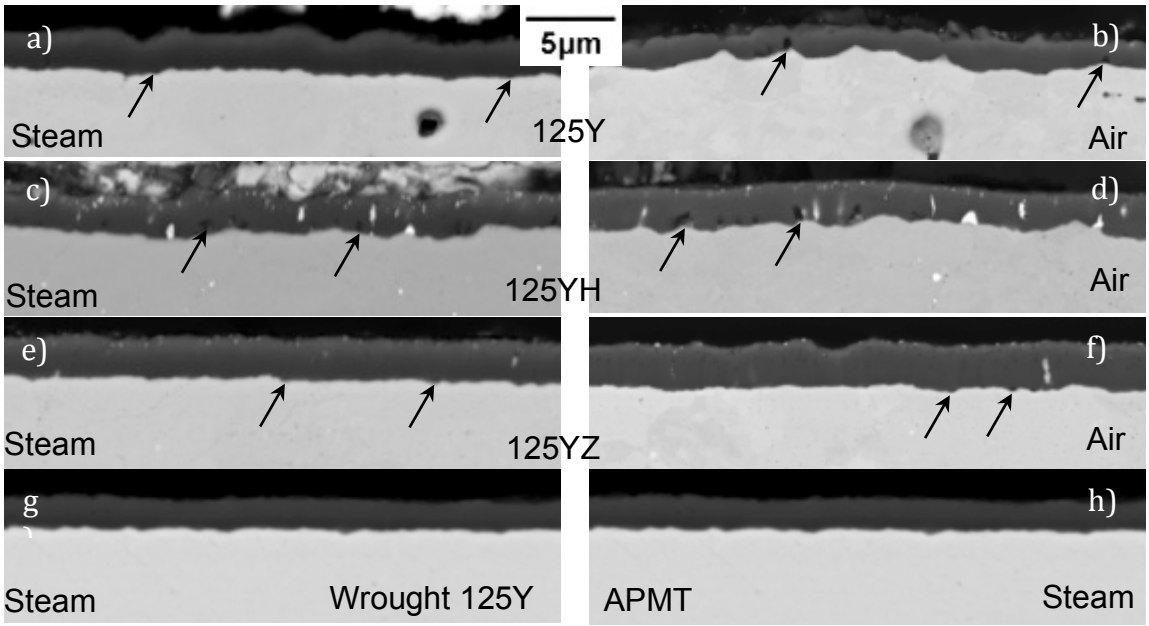

Figure 6. SEM BSE images of polished cross-sections after 4h exposures: a) 125Y in steam, b) 125Y in air, c) 125YH in steam, d) 125YH in air, e) 125YZ in steam, f) 125YZ in air, g) cast and rolled 125Y in steam, h) APMT in steam.

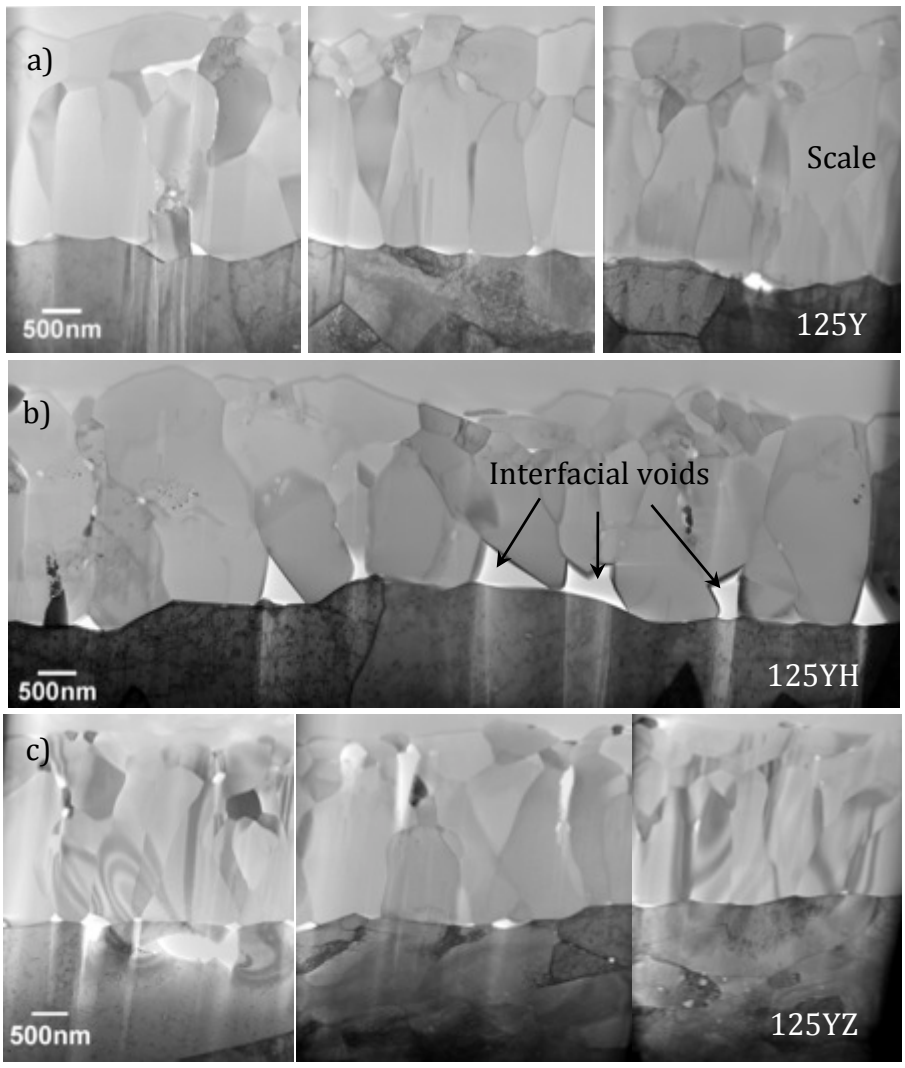

Figure 7. STEM bright field images of oxide cross-sections formed in steam after 4h at 1200°C on specimens of a) 125Y, b) 125YH, and c) 125YZ.

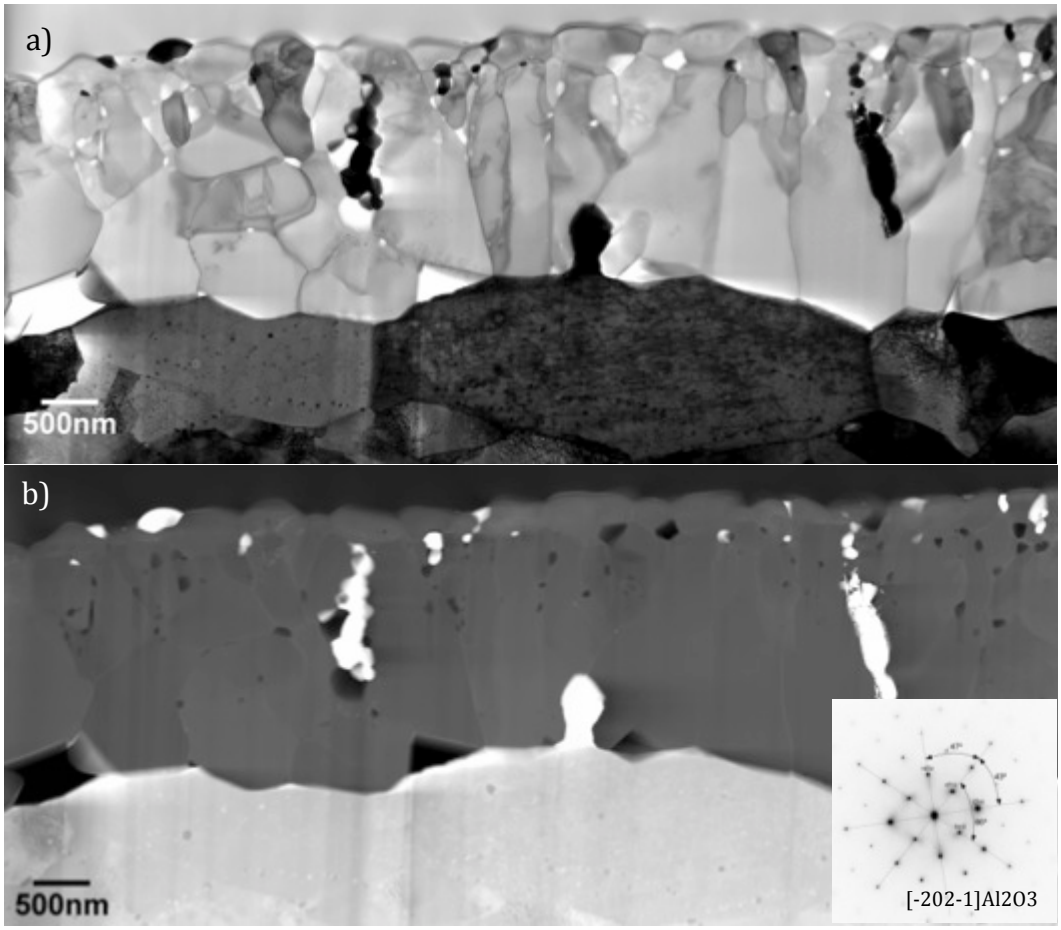

Figure 8. STEM (a) bright field and (b) annular dark field images of the scale cross-section formed on 125YH after 4h in air at 1200°C. Inset shows an indexed electron diffraction pattern from the inner oxide layer.

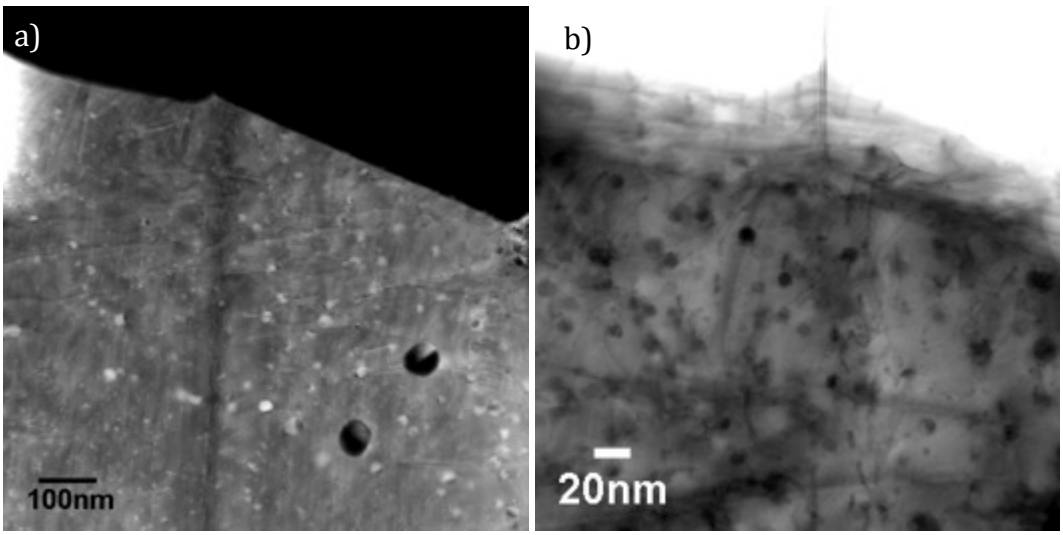

Figure 9. STEM (a) bright field and (b) annular dark field images of the 125YH substrate adjacent to the scale formed after 4h in air at 1200°C.

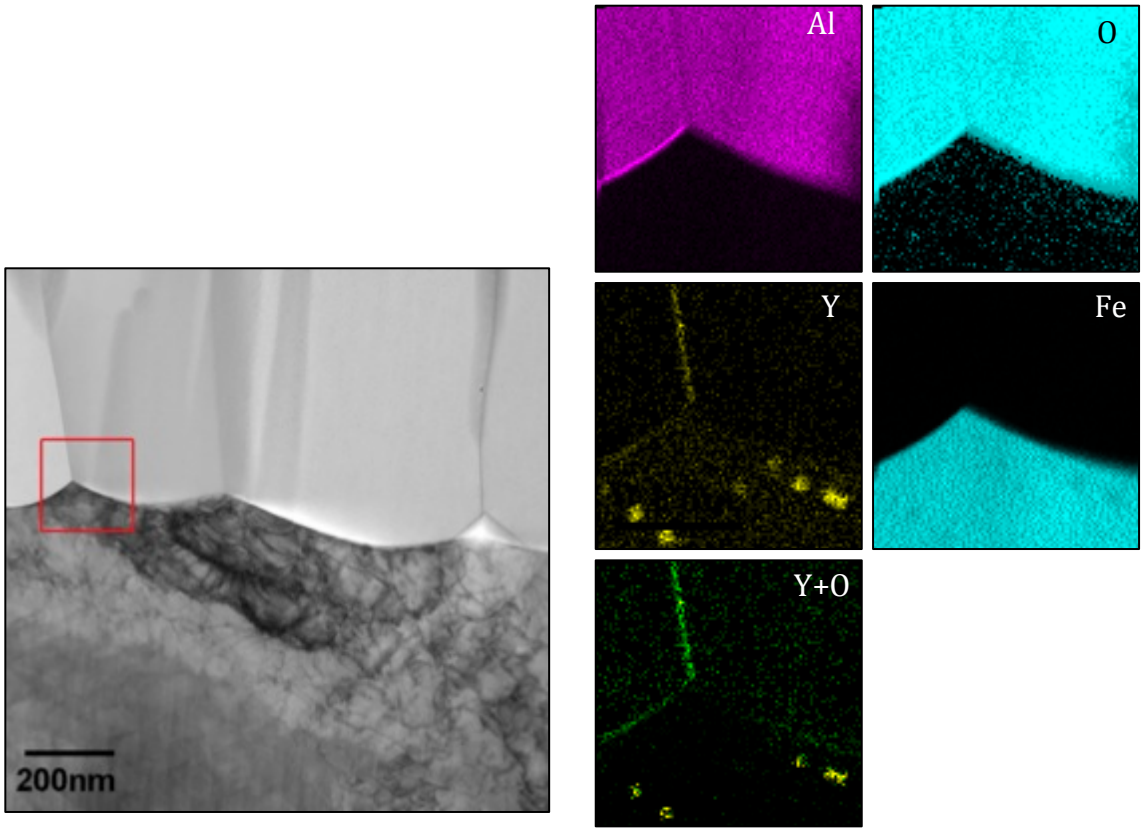

Figure 10. STEM (a) bright field image of the metal-oxide interface of 125Y after 4h at 1200°C in steam with EDS maps for Al, O, Y, Fe and Y+O map confirming presence of Y_2O_3 precipitates in the substrate near the thermally grown alumina scale.

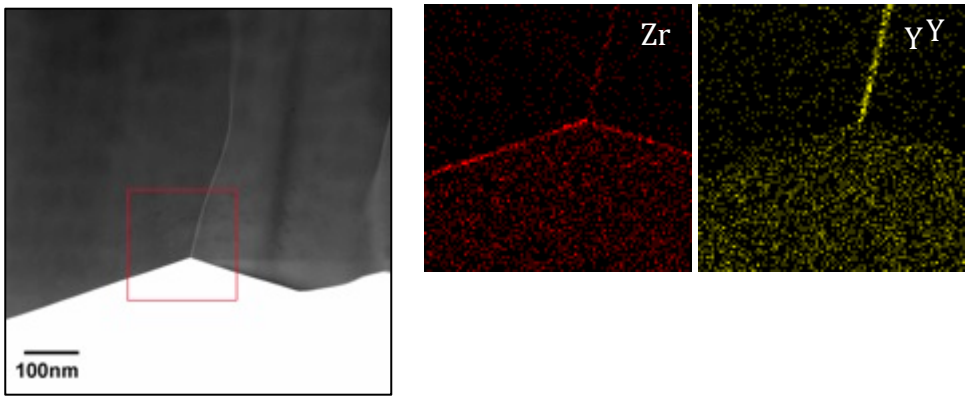

Figure 11. STEM (a) HAADF image of the oxide scale formed on the 125YZ specimen exposed for 4h at 1200°C in steam with the marked area used for EDS maps of Zr and Y.

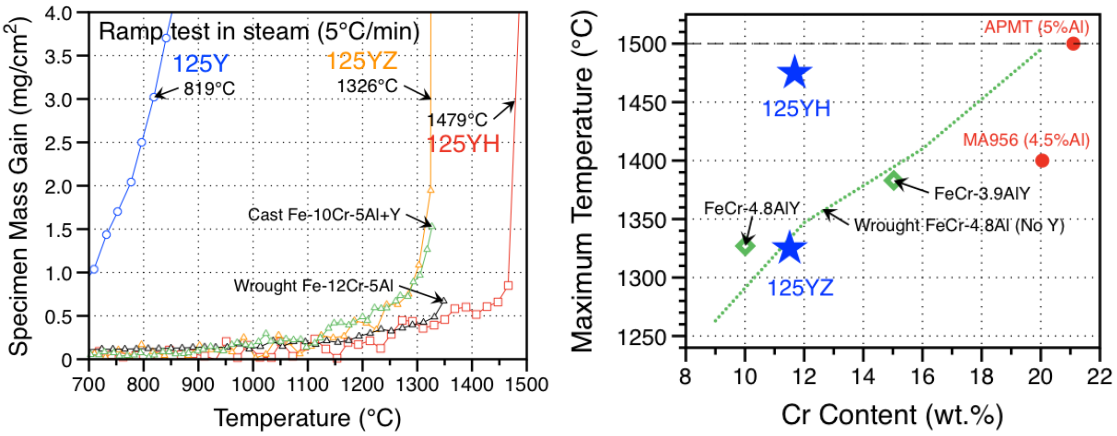

(a) (b)

Figure 12. a) Specimen mass gain as a function of temperature during the TGA ramp test in steam and (b) the maximum temperature capability as a function of alloy Cr content for the ODS alloys and other commercial and model alloys.